Iranian Journal of Chemistry and Chemical Engineering (IJCCE)

Synthesis of metallic Pt nanoparticles modified Bi_2WO_6 thin nanoplates with enhanced photodegradation of rhodamine B under visible light

Soraya Pinchujit, Anukorn Phuruangrat*
Division of Physical Science, Faculty of Science, Prince of Songkla University, Hat Yai, Songkhla 90112, Thailand
E-mails: 6510220074@psu.ac.th (S. Pinchujit)
phuruangrat@hotmail.com (A. Phuruangrat)

Surangkana Wannapop
Faculty of Science, Energy and Environment,
King Mongkut's University of Technology North Bangkok, Rayong Campus,
Rayong 21120, Thailand
E-mail: surangkana.w@sciee.kmutnb.ac.th (S. Wannapop)

Titipun Thongtem
Materials Science Research Center, Faculty of Science, Chiang Mai University,
Chiang Mai 50200, Thailand
Department of Chemistry, Faculty of Science, Chiang Mai University,
Chiang Mai 50200, Thailand
E-mail: ttpthongtem@yahoo.com (T. Thongtem)

Somchai Thongtem*
Materials Science Research Center, Faculty of Science, Chiang Mai University,
Chiang Mai 50200, Thailand
Department of Physics and Materials Science, Faculty of Science,
Chiang Mai University, Chiang Mai 50200, Thailand
E-mail: schthongtem@yahoo.com (S. Thongtem)

*Corresponding authors: phuruangrat@hotmail.com (A. Phuruangrat)
Tel. +66 (0)74 288374, Fax. +66 (0)74 288395 and
schthongtem@yahoo.com (S. Thongtem)
Tel. +66 (0)53 941915, Fax. +66 (0)53 941915

Abstract

Bi_2WO_6 synthesized by hydrothermal method and heterostructure 1-10wt% Pt/Bi_2WO_6 nanocomposites synthesized by sonochemical-assisted deposition method were studied for photocatalysis. The as-synthesized samples were characterized by X-ray diffraction (XRD), Fourier transform infrared (FTIR) spectroscopy, Raman spectrometry, X-ray photoelectron spectroscopy (XPS), transmission electron microscopy (TEM) and UV-visible diffuse reflectance spectroscopy (UV-vis DRS). The analytical results certified that metallic Pt nanoparticles were loaded on orthorhombic Bi_2WO_6 thin nanoplates and the visible light absorption of the nanocomposites was improved. The photocatalytic activities of the as-synthesized samples in degrading rhodamine B (RhB) were investigated under visible light for 180 min. The photodegradation efficiencies were 35.33%, 66.18%, 86.91% and 94.58% for 0%, 1%, 5% and 10% Pt/Bi_2WO_6 samples, respectively. The 10% Pt/Bi_2WO_6 nanocomposites have the highest photocatalytic activity because the Pt nanoparticles have the highest activity in harvesting visible light and the strongest surface plasmon resonance (SPR) effect. A possible mechanism for photocatalysis, main active radicals of the photodegradation process and recyclability of the heterostructure Pt/Bi_2WO_6 nanocomposites were also investigated in this research.

Keywords: *Pt/Bi_2WO_6; Photocatalysis; Recyclability; Main active radicals*

1. Introduction

In the past decades, photocatalysis has attractive potential applications in degrading organic contaminants due to its complete mineralization, simplicity, high efficiency, including mild temperature and pressure [1-4]. Titanium dioxide with a wide band gap of 3.2 eV has become one of the most important photocatalysts [5-7]. It is still having some key technical problems in photocatalytic technology because it has low utilization of solar energy and quantum yield and is active only UV light [5-8]. Thus, the development of visible-light-responsive photocatalyst is the main purpose to take up visible light of about 43% of the solar energy as compared with the UV light of about 4% [2, 7-9].

Bismuth tungstate (Bi_2WO_6), a narrow band gap semiconductor, has become the focus in the field of photocatalysis and was reported as the effective degradation for organic pollutants in water, such as methyl orange [9, 10], congo red [9], rhodamine B (RhB) [11-13], methylene blue (MB) [14-16], benzoic acid [15], phenol [17] and tetracycline [18, 19]. Bi_2WO_6, a typical Aurivillius oxide, is composed of accumulated layers of fluorite-like $[Bi_2O_2]^{2+}$ with corner-sharing perovskite-like $[WO_4]^{2-}$ which can promote high mobility of photo-generated charge carriers and improve photocatalytic reaction [1, 9, 20-22]. Nevertheless, the photocatalytic efficiency of Bi_2WO_6 is low and the rate of photogenerated carrier recombination is high [1, 2, 6, 23, 24]. Therefore, increasing in the separation of photogenerated carriers is the key purpose for photocatalyst with enhanced activity [1, 6, 25].

Recently, noble metal was used to improve photocatalytic efficiency because noble metal nanoparticles, a sink for electrons, can promote the interfacial diffusion process and surface plasmonic resonance (SPR) effect by forming Schottky barrier at the metal–semiconductor interface [2, 22-24, 26, 27]. For example, Liu et al. claimed that Au/Bi_2WO_6 nanosheet-based microspheres played the role in the degradation of phenol under visible light higher than Bi_2WO_6. They reported that Au nanoparticles acted as electron accepters to promote electron–hole separation and improve the photocatalytic efficiency [2]. Haiyan et al. succeeded in synthesizing of heterostructure Ag/Bi_2WO_6 composites by simple UV radiation method [26]. The heterostructure Ag/Bi_2WO_6 composites had the high photodegradation of RhB, MB and methyl red under visible radiation and were attributed to the difference in Fermi level of Ag nanoparticles and Bi_2WO_6. According to the previous reports, noble metal (Ag and Pd) and bimetallic (AgPd and PdAg) nanoparticles loaded on thin Bi_2WO_6 photocatalyst can lead to increase the photocatalytic activity of Bi_2WO_6 under visible radiation due to the formation of Schottky barrier of metallic nanoparticle – Bi_2WO_6 and plasmon resonance effect of noble metal nanoparticles (8, 24, 28-30).

In this research, heterostructure Pt/Bi_2WO_6 nanocomposites were synthesized by sonochemical-assisted deposition method. Their phase, structure, morphology and optical properties were analyzed. Effect of Pt nanoparticles loaded on Bi_2WO_6 thin nanoplates on the photodegradation of rhodamine B under visible radiation was investigated and discussed. A possible mechanism and recycle stability of the nanocomposites in degrading RhB were also proposed and discussed.

2. Experiment

2.1 Chemical reagents

Bismuth (III) nitrate pentahydrate ($Bi(NO_3)_3{\cdot}5H_2O$, ACS reagent, ≥98.0%), sodium tungstate dihydrate ($Na_2WO_4{\cdot}2H_2O$, ACS reagent, ≥99%) and chloroplatinic acid hydrate ($H_2PtCl_6{\cdot}xH_2O$, ≥99.9%) were purchased from Sigma-Aldrich Chemical Corporation. Rhodamine B ($C_{28}H_{31}ClN_2O_3$, ≥95%) was purchased from Loba Chemie Pvt. Ltd. They were used without further purification.

2.2 Preparation method

To prepare thin Bi_2WO_6 nanoplates, 0.01 mol $Bi(NO_3)_3 \cdot 5H_2O$ and 0.005 mol $Na_2WO_4 \cdot 2H_2O$ were dissolved in 100 ml reverse osmosis (RO) water. The solution was adjusted the pH to 6 by 3 mol/l NaOH and was hydrothermally heated at 180 ^oC for 20 h. The as-synthesized Bi_2WO_6 thin nanoplates were separated by filtering, washed and dried for further synthesis. In the end, each of 1%, 5% and 10% $H_2PtCl_6 \cdot xH_2O$ by weight was dissolved in 100 ml ethylene glycol and followed by the addition of 2.50 g Bi_2WO_6 thin nanoplates. The system was vibrated in a 240 W ultrasonic bath for 60 min and the as-synthesized heterostructure Pt/Bi_2WO_6 nanocomposites were collected for further characterization.

2.3 Characterization

Phase and structure of the samples were analyzed by a Philips X'Pert MPD X-ray diffractometer (XRD) using Cu K_α as an X-ray source. Raman and Fourier transform infrared (FTIR) spectra were analyzed by a HORIBA JOBIN YVON T64000 Raman spectrometer using Ar green laser source of 514.5 nm wavelength and a BRUKER TENSOR 27 Fourier transform infrared spectrometer. Their morphologies were characterized by a JEOL JEM-2010 transmission electron microscope (TEM) at an operating voltage of 200 kV. The chemical composition and oxidation state of elements containing in the samples were analyzed by an X-ray photoelectron spectrophotometer (XPS, Axis Ultra DLD, Kratos Analytical Ltd) using Al K_α radiation at 1486.6 eV and calibrated by C 1s at 285.1 eV. The UV-visible diffuse reflectance spectra (DRS) were analyzed by a UV-vis DRS Shimadzu UV-2600 spectrometer.

2.4 Photocatalysis

Fig. 1 shows a schematic diagram for photocatalysis of Bi_2WO_6 nanoplates and heterostructure Pt/Bi_2WO_6 nanocomposites in degrading RhB under visible light. General properties of RhB were summarized in Table 1 [31-33]. Each 0.2 g of Bi_2WO_6 and heterostructure Pt/Bi_2WO_6 samples was suspended in 200 ml of $1x10^{-5}$ mol/l RhB solutions under magnetic stirring. Before irradiation, the solution was stirred in the dark for 30 min and irradiated by visible light of a xenon lamp with a 420 nm cutoff filter.

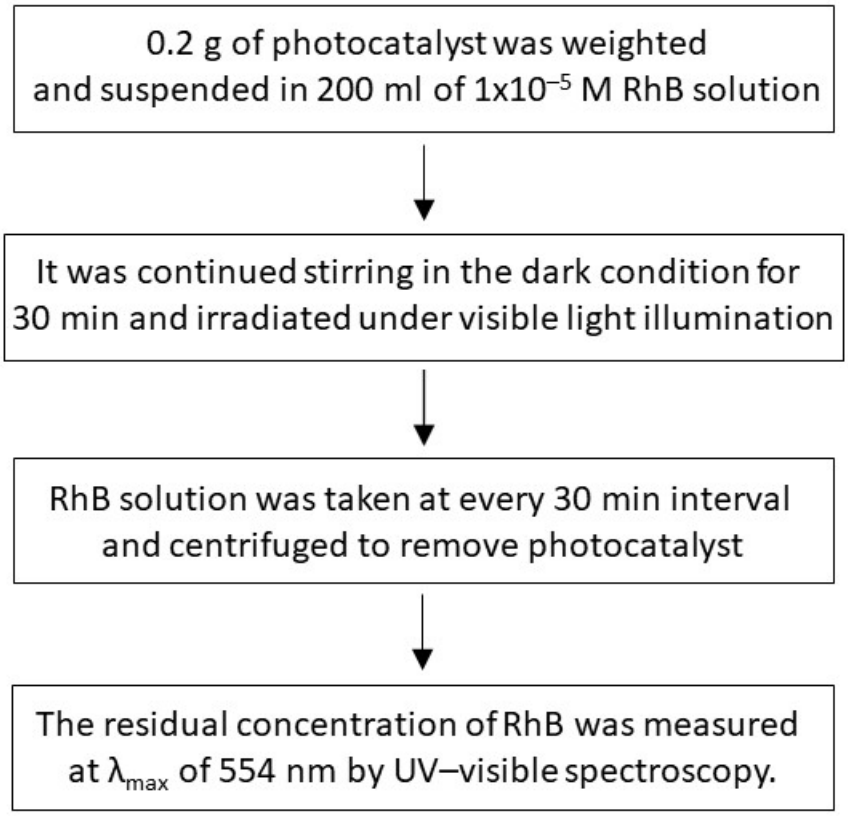

Fig. 1 The photocatalytic process of Bi_2WO_6 and heterostructure Pt/Bi_2WO_6 samples in the degradation of RhB.

Table 1. The properties of RhB.

Properties of RhB	**Values**
Chemical formula	$C_{28}H_{31}ClN_2O_3$
IUPAC name	9-(2-carboxyphenyl)-6-(diethylamino)N,N-diethyl-3H-xanthen-3-iminium chloride
pKa	50 (20 °C)
λ_{max} (nm)	554 nm
Class	Triphenylmethane
Name (CI)	Basic Violet 10; Brilliant Pink B
Color index (CI) number	45170

During the photocatalysis, 5 ml RhB solution was taken from the photocatalytic reactor every 30 min interval. The sample solution was centrifuged to separate the solid photocatalyst from the liquid solution and analyzed the residual concentration of RhB solution by a PerkinElmer Lambda 25 UV–visible spectrometer at the maximum absorption wavelength (λ_{max}) of 554 nm. The decolorization efficiency was calculated by the following.

$$\text{Decolorization efficiency (\%)} = \frac{C_o - C_t}{C_o} \text{x100} \qquad (1)$$

C_o and C_t are the RhB concentration of the solution before and after light irradiation within a period of time (t).

3. Results and discussion

The XRD pattern of pure Bi_2WO_6 sample (Fig. 2) was composed of diffraction peaks at 2θ = 28.29°, 32.91°, 47.18°, 55.97° and 58.63° which were indexed to the (131), (200), (260), (191) and (133) planes of a typical orthorhombic Bi_2WO_6 according to the JCPDS no. 39-0256 [34]. No other impurities were detected in the XRD pattern of Bi_2WO_6, indicating that the as-prepared Bi_2WO_6 sample was pure phase. XRD patterns of Pt/Bi_2WO_6 nanocomposites show the diffraction patterns of a typical orthorhombic Bi_2WO_6 structure with an additional diffraction peak at 2θ = 39.75° of the (111) peak of face centered cubic Pt structure (marked with ■) according to the JCPDS no. 04-0802 [34]. They should be noted that the diffraction peaks of Bi_2WO_6 in Pt/Bi_2WO_6 nanocomposites were slightly shifted w.r.t the pure Bi_2WO_6 phase. Possibly, the shift was caused by the interface of FCC Pt structure and orthorhombic Bi_2WO_6 structure. The average crystallite size of metallic Pt nanoparticles containing in the as-prepared 10% Pt/Bi_2WO_6 nanocomposites calculated by the Scherrer formula [8, 14, 21, 24, 35] was 12 nm.

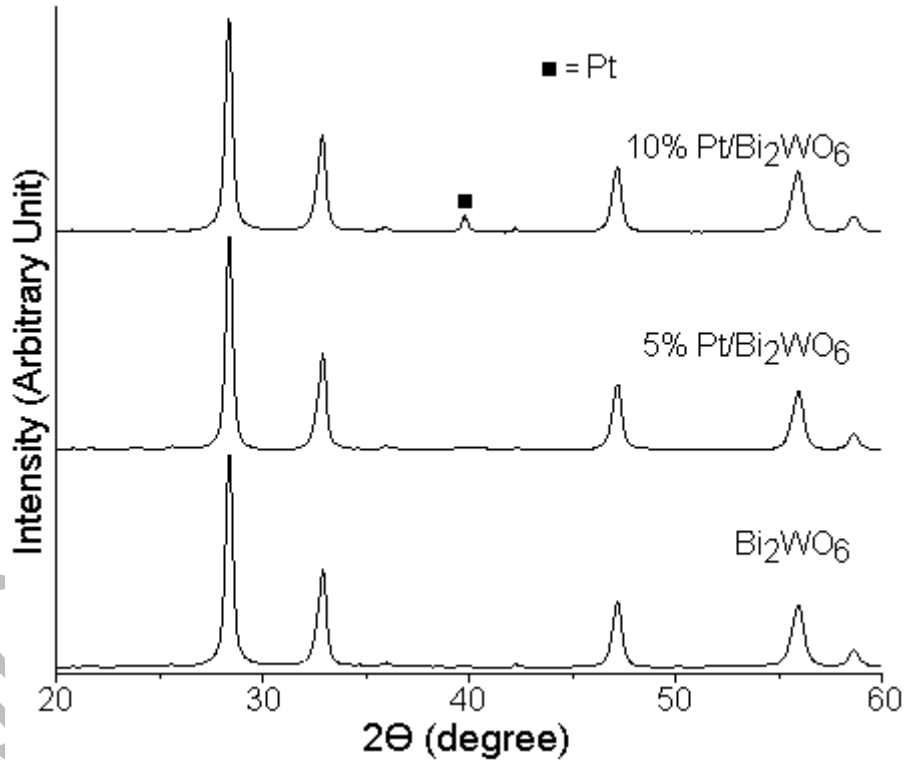

Fig. 2 XRD patterns of Bi_2WO_6 and heterostructure Pt/Bi_2WO_6 samples.

The crystal structure of Bi_2WO_6 Aurivillius-type structure with I4/mmm contains layers of perovskite-like $(WO_4)^{2-}$ and fluorite-like $(Bi_2O_2)^{2+}$ lying normal to the [001] direction [1, 8, 11, 18, 21, 36, 37]. The $2A_{1g} + B_{1g} + 3E_g$ modes are Raman active and the $4A_{2u} + 5E_u$ modes are IR active [31-34]. They are classified into symmetric (A_{1g}) and asymmetric ($A_{2u} + E_u$) stretching vibrations of WO_6 octahedrons, stretching and bending vibration ($B_{1g} + E_g + A_{2u} + E_u$) of $(Bi_2O_2)^{2+}$ layers, bending vibration ($E_g + 2E_u + A_{2u} + B_{2u}$) of WO_6 octahedrons, translational motion ($A_{1g} + E_g$) of Bi^{3+} and vibration involving translational motion ($A_{2u} + E_u$) of Bi^{3+} and

W^{6+} ions [36-39]. Fig. 3a shows the FTIR spectra of Bi_2WO_6 and Pt/Bi_2WO_6 samples diluted by KBr over the wavenumber range of 400–4000 cm^{-1}. The pure Bi_2WO_6 sample shows the Bi–O stretching at 823 cm^{-1} and W–O stretching at 733 cm^{-1}. The asymmetric bridge W–O–W stretching mode was detected at 583 cm^{-1} [10, 20, 21, 24, 36, 37]. The FTIR spectra of Pt/Bi_2WO_6 nanocomposites show the slight shift of wavenumbers with respect to that of the pure Bi_2WO_6 sample due to the strong interaction of metallic Pt and Bi_2WO_6 nanoparticles [21, 24]. The broad FTIR bands at 3200-3400 cm^{-1} were detected in all samples which were assigned to the stretching vibration of O–H bonds of adsorbed water on the top surface [10, 20, 21, 24, 36, 37].

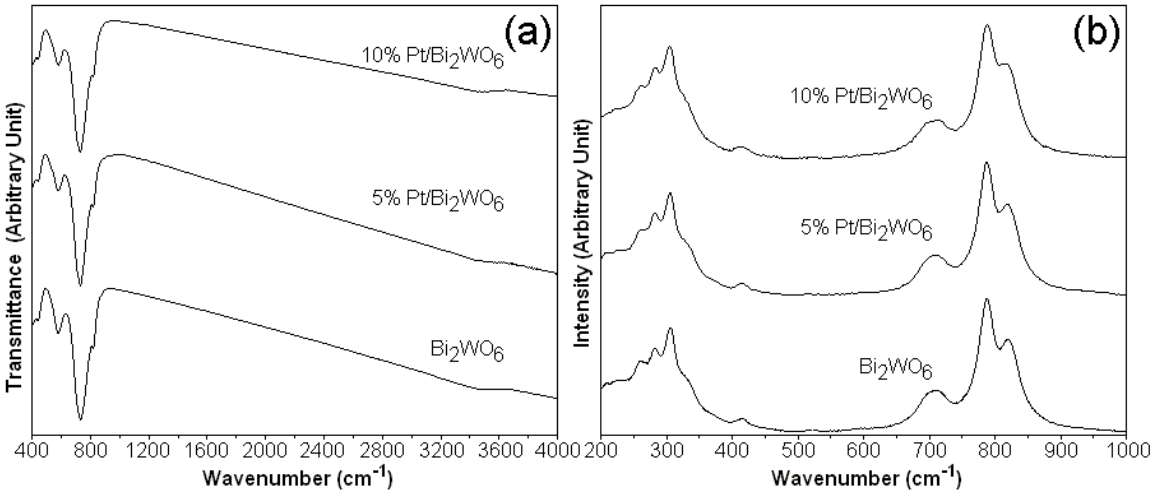

Fig. 3 (a) FTIR and (b) Raman spectra of Bi_2WO_6 and Pt/Bi_2WO_6 samples.

Fig. 3b shows the Raman spectra of Bi_2WO_6 and Pt/Bi_2WO_6 samples. The Raman vibration of Bi_2WO_6 below 600 cm^{-1} is originated from the WO_6 bending mode coupled with Bi–O bending mode of the polyhedrons [14, 21, 23, 36, 37]. The vibration of W–O stretching mode was detected at 600–1000 cm^{-1} [14, 21, 23, 36, 37]. The Raman peaks at 259 (E_u), 280 (E_g), 305 (E_g) and 416 (E_u) cm^{-1} correspond to the bending vibration of WO_6 octahedrons. The Raman shoulder at 331 cm^{-1} corresponds to the bending of Bi–O polyhedrons (B_{1g}) [14, 21, 23, 36, 37]. The shoulder of B_2WO_6 at 707 cm^{-1} was related to the asymmetric stretching mode of WO_6 octahedrons (E_u) [14, 21, 23, 36, 37]. The Raman peaks at 787 and 814 cm^{-1} were detected in Bi_2WO_6 which were assigned to the symmetric and antisymmetric stretching of terminal O–W–O groups (A_g), respectively [14, 21, 23, 36, 37]. They should be noted that the Raman peaks of Pt/Bi_2WO_6 nanocomposites exhibit no difference with respect to those of the as-prepared Bi_2WO_6 sample. Possibly, the sample contains very low content of Pt nanoparticles.

Fig. 4a is the TEM image of the as-prepared Bi_2WO_6 sample. The sample was composed of uniform nanoplates with size of 50-80 nm. The high resolution transmission electron microscopic (HRTEM) image of a single Bi_2WO_6 nanoplate (inserted in Fig. 4a) reveals the lattice spaces of 0.273 and 0.272 nm corresponding to the (200) and (002) planes of orthorhombic Bi_2WO_6 structure.

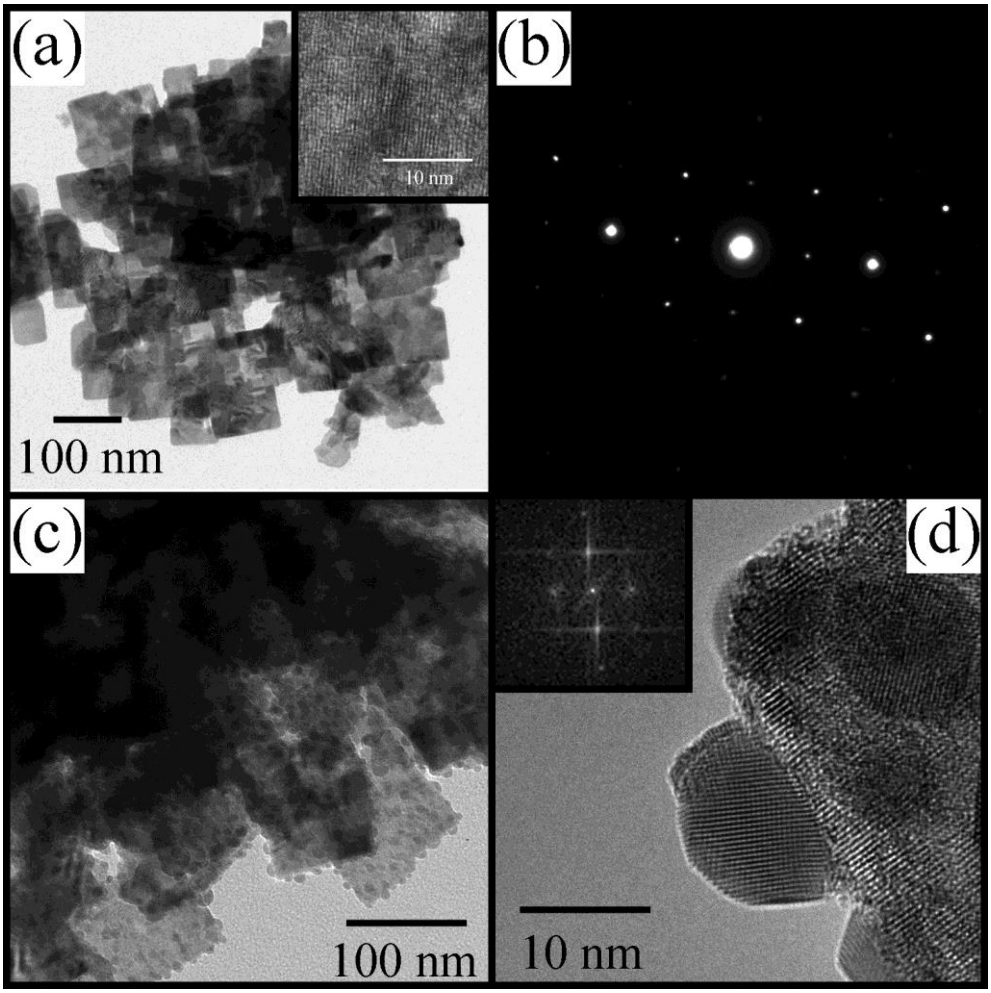

Fig. 4 TEM and HRTEM images, and SAED and FFT patterns of (a, b) Bi_2WO_6 and (c, d) heterostructure 10% Pt/Bi_2WO_6 nanocomposites.

The selected area electron diffraction (SAED) of a single Bi_2WO_6 nanoplate (Fig 4b) shows the bright spots of electron diffraction, corresponding to the (020), (220) and (200) planes of orthorhombic Bi_2WO_6 structure with zone axis of [001]. A single thin Bi_2WO_6 nanoplate preferentially grew along the (010) plane because the (010) plane of orthorhombic Bi_2WO_6 has an atom density higher than other planes [8, 11, 21, 40, 41]. The SAED and HRTEM results indicate that the Bi_2WO_6 nanoplates were built of fluorite-like $(Bi_2O_2)^{2+}$ and perovskite-like $(WO_4)^{2-}$ in the [001] direction [1, 8, 11, 18, 21]. Fig. 4c shows the TEM image of 10% Pt/Bi_2WO_6 nanocomposites which were composed of Pt nanoparticles with particle size of 8-10 nm supported on the surface of Bi_2WO_6 nanoplates. Fig. 4d shows the HRTEM image of 10% Pt/Bi_2WO_6 nanocomposites which show the interface of Pt nanoparticles and Bi_2WO_6 nanoplates. Clearly, the Pt nanoparticles were excellently adhered on the surface of Bi_2WO_6 nanoplates. The HRTEM image of 10% Pt/Bi_2WO_6 nanocomposites certifies the formation of Pt/Bi_2WO_6 heterojunctions and shows the lattice space of 0.273 nm for (200) crystallographic planes of orthorhombic Bi_2WO_6 structure and lattice space of 0.226 nm for (111) crystallographic plane of FCC Pt structure. In addition, a fast Fourier transform (FFT) pattern of Pt nanoparticles (inserted in Fig. 4d) indicated that the Pt nanoparticles are good single crystal.

The surface composition and oxidation state of Bi_2WO_6 and Pt/Bi_2WO_6 samples analyzed by XPS are shown in Fig. 5. The full survey XPS spectrum of Bi_2WO_6 is mainly composed of Bi, W and O elements while

the full survey XPS spectrum of Pt/Bi_2WO_6 nanocomposites is composed of additional Pt element. The high resolution XPS spectrum of Pt/Bi_2WO_6 nanocomposites shows two binding energy peaks at 71.16 eV and 74.54 eV which are assigned to the Pt $4f_{7/2}$ and Pt $4f_{5/2}$ core levels. They certified the presence of metallic Pt^0 in heterostructure 10% Pt/Bi_2WO_6 nanocomposites [7, 23, 42, 43]. The binding energies of Pt $4f_{7/2}$ and Pt $4f_{5/2}$ core levels of Pt^{2+} were detected at 72.01 eV and 75.66 eV because PtO was synthesized during XPS analysis [42, 43]. The two prominent high resolution binding energies of Bi 4f peaks were detected at 159.34 and 164.64 eV for Bi_2WO_6 and 159.49 eV and 164.79 eV for 10% Pt/Bi_2WO_6 with a 5.3 eV spin–orbit splitting value. They were ascribed to Bi $4f_{7/2}$ and Bi $4f_{5/2}$ core levels which certified that Bi mainly exists in the Bi^{3+} form [7, 8, 10, 16, 18, 20, 21, 24, 36]. The high resolution binding energies of W 4f core levels were detected at 35.59 and 37.73 eV for Bi_2WO_6 and 35.66 eV and 37.86 eV for 10% Pt/Bi_2WO_6. They correspond to the W $4f_{7/2}$ and W $4f_{5/2}$ core levels with the presence of W^{6+} in Bi_2WO_6 lattice [8, 10, 16, 18, 20, 21, 24, 36]. The asymmetric high resolution binding energy of O 1s was disintegrated into four peaks at 530.13, 530.97, 532.21 and 533.41 eV for Bi_2WO_6 and three peaks at 530.48, 532.04 and 533.50 eV for 10% Pt/Bi_2WO_6. They were attributed to Bi–O (530.13 eV for Bi_2WO_6 and 530.48 for 10% Pt/Bi_2WO_6) and W–O (530.97 eV for Bi_2WO_6) and adsorbed oxygen species of OH^- (532.21 eV for Bi_2WO_6 and 532.04 for 10% Pt/Bi_2WO_6) and H_2O (533.41 eV for Bi_2WO_6 and 533.50 eV for 10% Pt/Bi_2WO_6) [8, 10, 16, 18, 20, 21, 24, 36]. The analytical results suggest that there were metallic Pt^0 containing in the composites and ionic Pt^{2+} was synthesized during the XPS analysis.

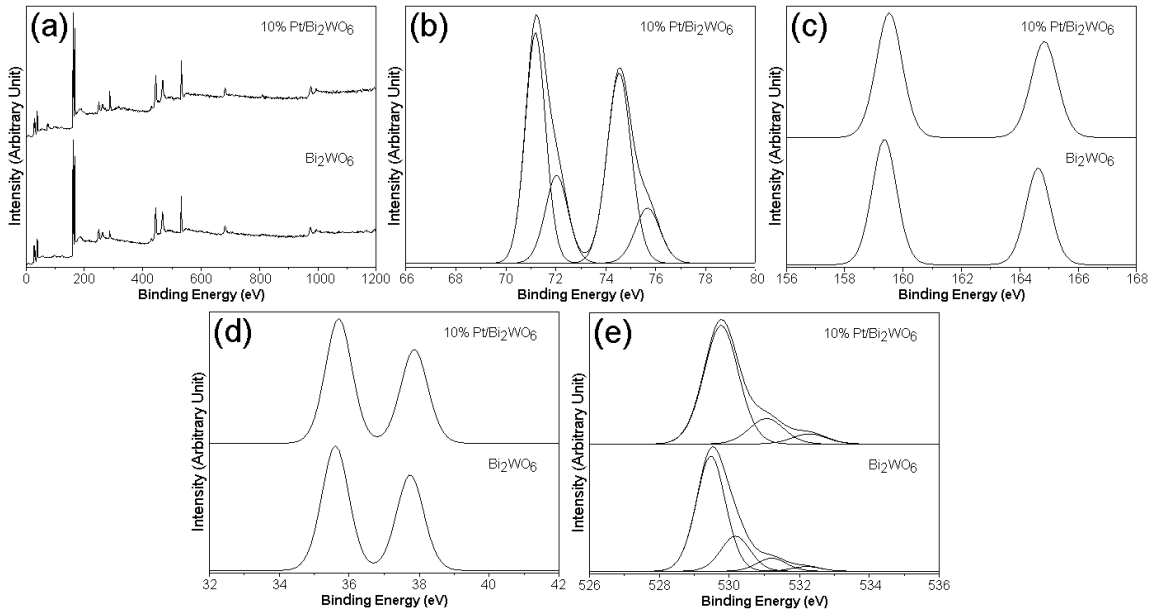

Fig. 5 XPS spectra of (a) full survey scan and high-resolution XPS spectra of (b) Pt 4f, (c) Bi 4f, (d) W 4f and (e) O 1s of Bi_2WO_6 and 10% Pt/Bi_2WO_6 samples.

Fig. 6 shows the UV–visible DRS spectrum of the Bi_2WO_6 and Pt/Bi_2WO_6 samples. The DRS spectrum of as-prepared Bi_2WO_6 sample shows the EM wave ranging from strong UV to visible light with the 396 nm absorption edge of the intrinsic band gap of Bi_2WO_6 [10, 13, 14, 17, 23, 27]. Obviously, the DRS spectrum of Pt/Bi_2WO_6 nanocomposites has high intensity in visible light region with absorption edge of 404 nm for 5% Pt/Bi_2WO_6 and 407 nm for 10% Pt/Bi_2WO_6. They were attributed to the SPR effect of Pt nanoparticles that led to improve the photocatalytic activity of Bi_2WO_6 under visible light [2, 7, 22, 23, 26, 27, 44]. The band gaps of Bi_2WO_6 and Pt/Bi_2WO_6 samples were estimated by the $E_g = 1240/\lambda$ equation [23, 45, 46]. Their band gaps were

decreased from 3.13 eV for Bi_2WO_6 to 3.06 eV for 5% Pt/Bi_2WO_6 and 3.04 eV for 10% Pt/Bi_2WO_6 caused by the introduction of localized energy levels in the Bi_2WO_6 band gap by Pt nanoparticles [2, 7, 22, 23, 26, 27, 44].

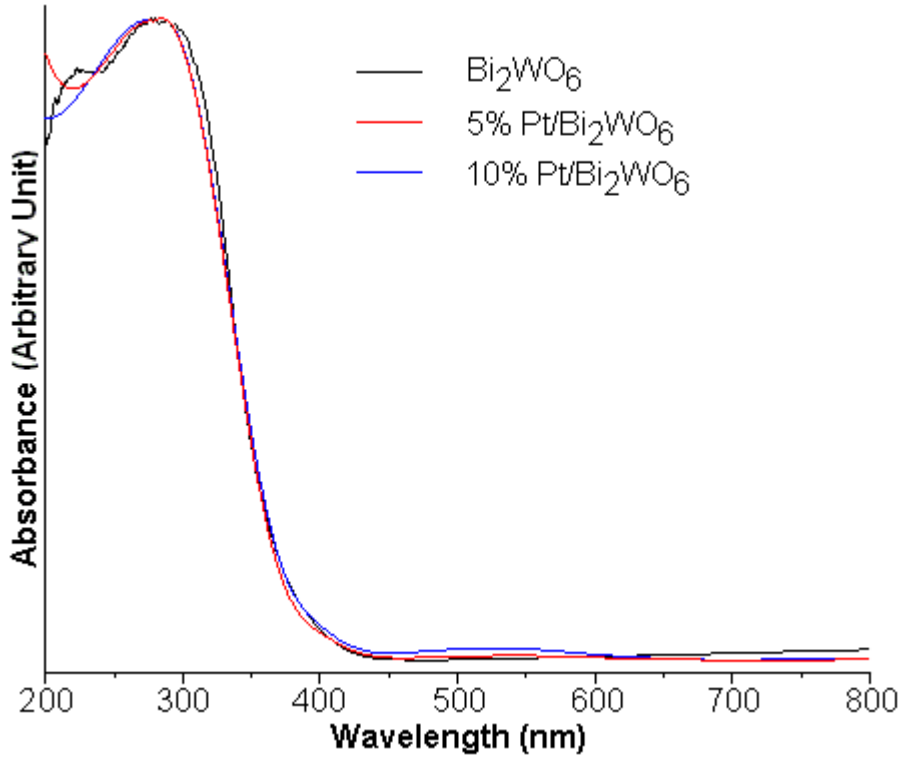

Fig. 6 DRS spectra of as-prepared Bi_2WO_6 and Pt/Bi_2WO_6 samples.

In order to investigate the photocatalytic activities of Bi_2WO_6 and Pt/Bi_2WO_6 samples, RhB dye was selected as the pollutant model because RhB can be monitored by UV-visible spectroscopy and is very stable under visible light. According to the previous report, the zeta potential of Bi_2WO_6 was at the pH of 5.32 and the surface charge of Bi_2WO_6 was neutral. The surface charge of Bi_2WO_6 was positive for the pH < 5.32 and was changed to negative for the pH > 5.32 [47]. The cationic RhB was adsorbed on the surface of Bi_2WO_6. Therefore, the RhB was selected as a dye model for this photocatalytic study. Fig. 7 shows time-dependent UV–visible spectra of RhB solutions over Bi_2WO_6 and Pt/Bi_2WO_6 samples illuminated by visible light. The UV-visible absorption of RhB was dramatically decreased with the increase of irradiation time for both Bi_2WO_6 and Pt/Bi_2WO_6 samples. The intensity of maximum absorption of RhB at 554 nm in the presence of Pt/Bi_2WO_6 nanocomposites was decreased faster than that in the presence of Bi_2WO_6. Thus, the RhB degradation over Pt/Bi_2WO_6 nanocomposites is faster than that over Bi_2WO_6. At the end of 180 min irradiation time, λ_{max} of RhB over 10% Pt/Bi_2WO_6 nanoplates was significantly shifted to 498 nm due to N-de-ethylation and RhB was completely degraded [7, 12, 21, 24].

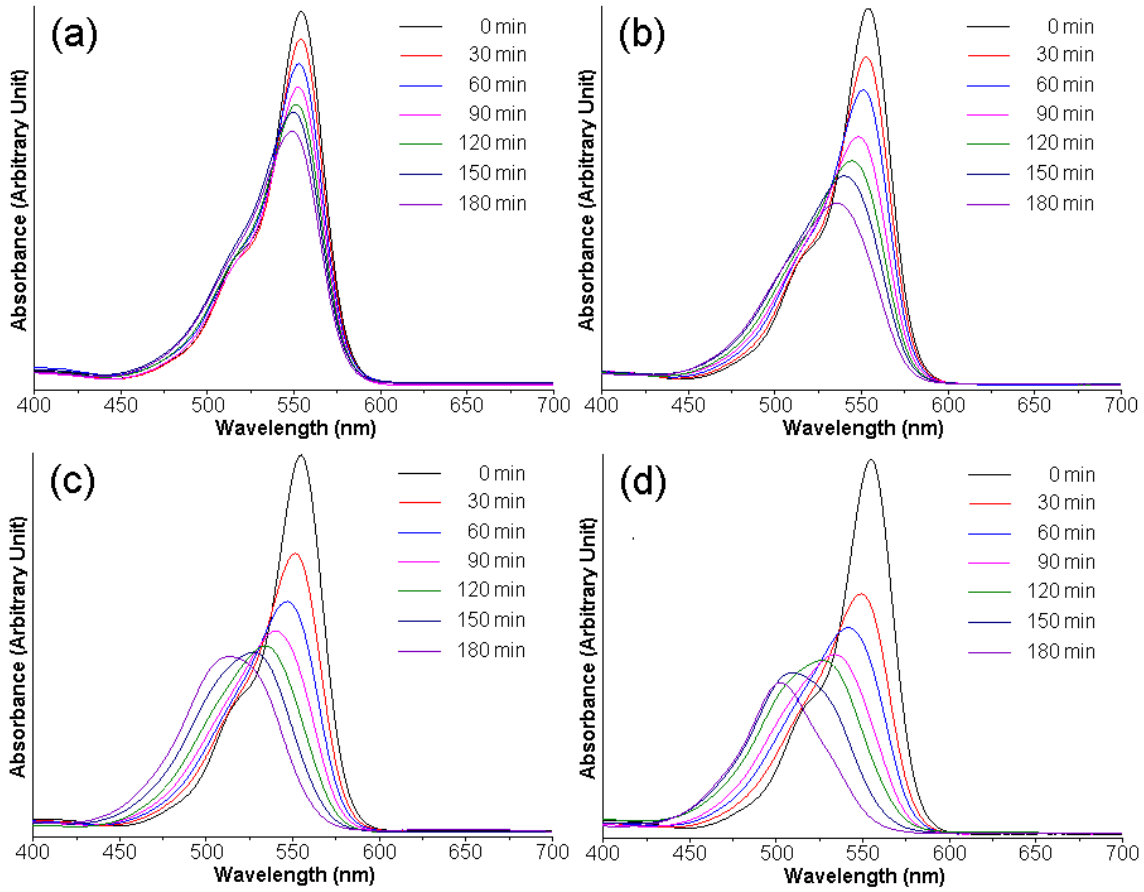

Fig. 7 Temporal evolution of UV-visible spectra of RhB photocatalyzed by (a) Bi_2WO_6, (b) 1% Pt/Bi_2WO_6, (c) 5% Pt/Bi_2WO_6 and (d) 10% Pt/Bi_2WO_6 samples.

Fig. 8a shows the photocatalytic efficiency of Bi_2WO_6 and heterostructure Pt/Bi_2WO_6 samples in degrading RhB within 180 min. The results indicate that the photodegradation efficiency was increased with increasing in the weight content of the loaded Pt and the irradiation time. The weight content of Pt has the influence on the photocatalytic activity of Bi_2WO_6. At the end of 180 min irradiation time, the photodegradation efficiencies were 35.33%, 66.18%, 86.91% and 94.58% for 0%, 1%, 5% and 10% Pt/Bi_2WO_6, respectively. The photodegradation efficiency of 10% Pt/Bi_2WO_6 nanocomposites was the highest because the Pt nanoparticles played the role in the highest harvesting visible light and having the strongest SPR effect [2, 7, 8, 24, 26, 27]. Comparing the photocatalytic performance of the 10% Pt/Bi_2WO_6 nanocomposites of the present work and those of other samples of the previous reports, the 10% Pt/Bi_2WO_6 nanocomposites have the photocatalytic performance higher than other samples of the previous reports as the results summarized in Table 2. Thus, the 10% Pt/Bi_2WO_6 nanocomposites are the best candidate for dye degradation under visible radiation.

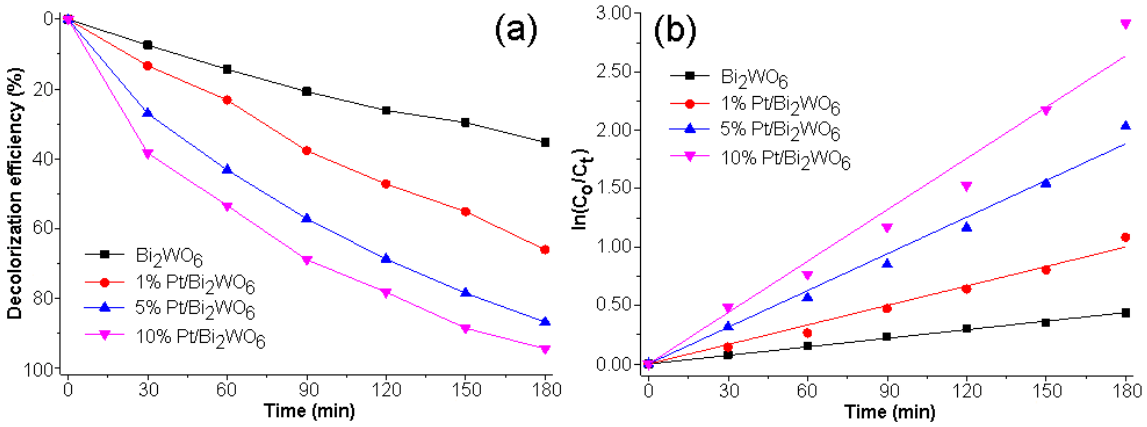

Fig. 8 (a) Decolorization efficiency and (b) pseudo-first-order plots for RhB degradation over Bi_2WO_6, 1% Pt/Bi_2WO_6, 5% Pt/Bi_2WO_6 and 10% Pt/Bi_2WO_6 samples illuminated by visible light.

Table 2. Photocatalytic performance of the present and previous reports.

Photocatalysts	**Photocatalytic performance**	**Refs.**
Bi_2WO_6	97.4%, 330 min	[5]
10% WO_3/Bi_2WO_6	78.1%, 150 min	[6]
Bi_2WO_6	84.87%, 120 min	[14]
Bi_2WO_6	99.87%, 160 min.	[16]
3% Au-doped Bi_2WO_6	96.25%, 240 min	[21]
5% $Ag_{0.9}Pd_{0.1}/Bi_2WO_6$	87.72%, 210 min	[31]
Bi_2WO_6@MoS_2/graphene Hybrids	~90%, 180 min	[48]
1.5% Er-doped Bi_2WO_6	~99%, 240 min	[49]
10% Pt/Bi_2WO_6	94.58%, 180 min	This work

The kinetic reactions for RhB degradation over as-prepared photocatalysts were investigated according to the Langmuir–Hinshelwood model [3, 7, 8, 12, 14, 18, 21, 24, 27]. Fig. 8b shows the plots of $\ln(C_o/C_t)$ versus reaction time. The plots corresponded with the linear lines and the photocatalytic performances of all samples followed pseudo-first-order kinetics [3, 7, 8, 12, 14, 18, 21, 24, 27]. The estimated reaction rate constants were 2.30×10^{-3}, 5.60×10^{-3}, 0.0104 and 0.0146 min^{-1} for 0%, 1%, 5% and 10% Pt/Bi_2WO_6, respectively. Among them, the 10% Pt/Bi_2WO_6 is the best photocatalyst. Within 180 min, the decolorization of RhB photocatalyzed by 10% Pt/Bi_2WO_6 nanocomposites prepared by sonochemical-assisted deposition method of our current work was compared with that photocatalyzed by 10% Pt/Bi_2WO_6 nanocomposites prepared by microwave-assisted deposition method of our previous work [50]. The decolorization efficiency of the current nanocomposites was 94.58% and that of the previous nanocomposites was 98.09%. The results show that the current decolorization efficiency is less than the previous one. Thus, the deposition frequency used for preparing the 10% Pt/Bi_2WO_6 nanocomposites played the role in the photodegradation rate of RhB.

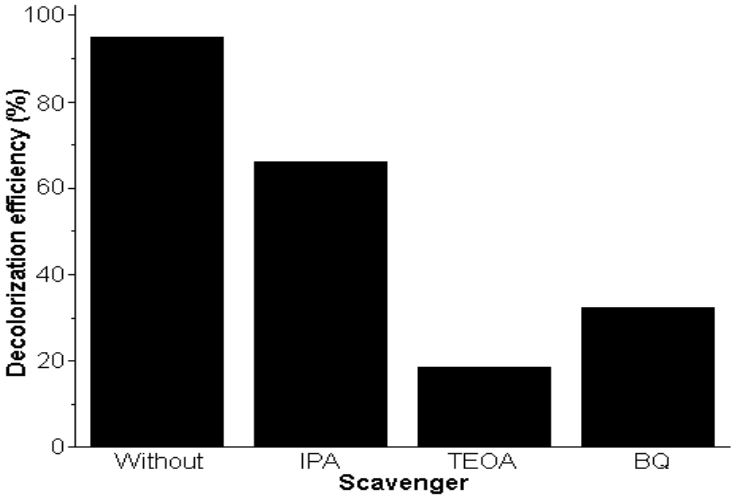

Fig. 9 Photodegradation efficiency of heterostructure 10% Pt/Bi_2WO_6 nanocomposites in degrading RhB solutions with and without IPA, TEOA and BQ scavengers.

In order to investigate the photocatalytic mechanism of Pt/Bi_2WO_6 nanocomposites, free radical trapping experiment was carried out using several scavengers: isopropyl alcohol (IPA) as a $^{\bullet}OH$ scavenger, triethanolamine (TEOA) as a h^+ scavenger and benzoquinone (BQ) as a $^{\bullet}O_2^-$ scavenger. They also contained in the RhB solutions during the photocatalysis [8, 21, 24, 51, 52]. Fig. 9 shows that the photodegradation efficiencies of 10% Pt/Bi_2WO_6 nanocomposites were decreased to 65.83%, 32.35% and 18.50% when IPA, BQ and TEOA were also added to the RhB solutions, respectively. In conclusion, the main active species used for RhB degradation are in sequence as follows: $h^+ >> {}^{\bullet}O_2^- > {}^{\bullet}OH$. On the basis of these results, the enhanced photodegradation of Pt/Bi_2WO_6 photocatalyst was also attributed to the SPR effect and harvest of visible light [2, 7, 8, 24, 27].

Fig. 10 shows the schematic diagram for photocatalytic performance of heterostructure Pt/Bi_2WO_6 nanocomposites.

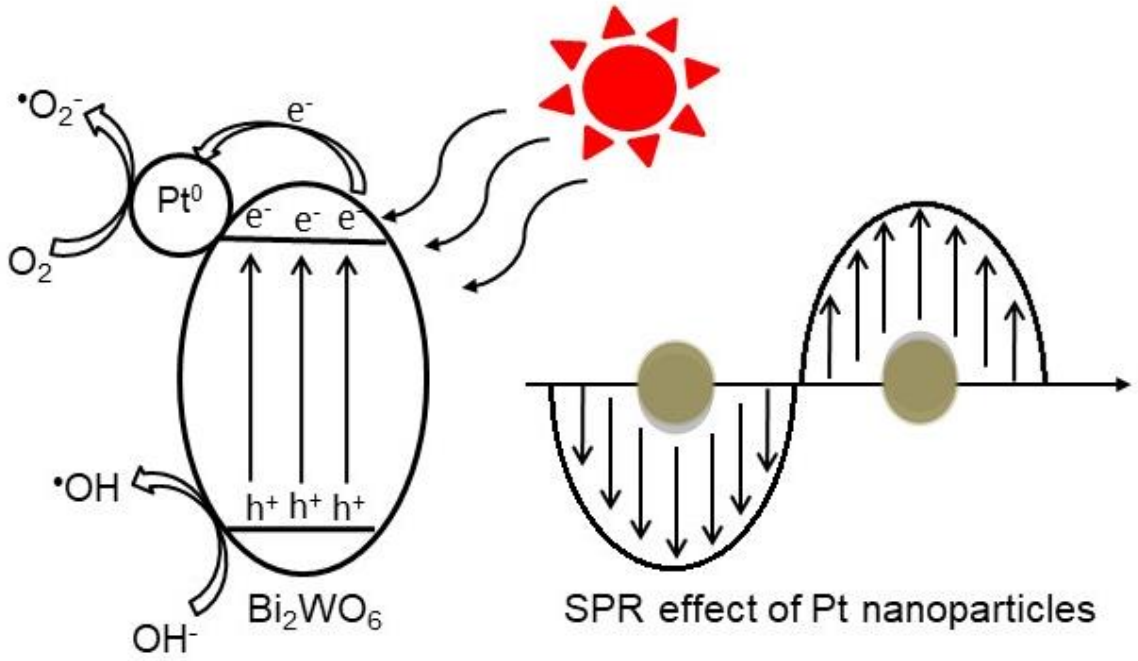

Fig. 10 Photocatalytic diagram of heterostructure Pt/Bi_2WO_6 nanocomposites illuminated by visible radiation.

Under visible light illumination, the Pt nanoparticles acted as electron acceptors to suppress electron–hole recombination and promoted interfacial charge diffusion [2, 7, 8, 24, 27, 36]. The photo-excited electrons on conduction band (CB) of Bi_2WO_6 diffused to the Pt nanoparticles through the Schottky barrier at the metal–semiconductor interface and the charge separation was improved [2, 7, 8, 24, 27, 36, 53]. Subsequently, the electrons were trapped by adsorbed O_2 in water to produce $^{\bullet}O_2^-$ radicals [2, 7, 8, 16, 24, 27, 31]. The photogenerated holes in the valence band (VB) of Bi_2WO_6 directly oxidized OH^- or water molecules to form $^{\bullet}OH$ active radicals [2, 7, 8, 16, 24, 27, 31, 54, 55]. Among these three species (h^+, $^{\bullet}O_2^-$ and $^{\bullet}OH$), they are able to separately transform the RhB dye into small inorganic compounds. The photocatalytic process of Pt/Bi_2WO_6 nanocomposites can be shown by the following.

$$Bi_2WO_6 + hv \rightarrow e^-_{CB} + h^+_{VB} \quad (2)$$

$$e^-_{CB} + Pt \rightarrow e^-_{Pt} \quad (3)$$

$$e^-_{Pt} + O_2 \rightarrow {}^{\bullet}O_2^- \quad (4)$$

$$h^+_{VB} + H_2O/OH^- \rightarrow {}^{\bullet}OH \quad (5)$$

$$Dye + h^+_{VB}/{}^{\bullet}O_2^-/{}^{\bullet}OH \rightarrow \text{Degraded products} \quad (6)$$

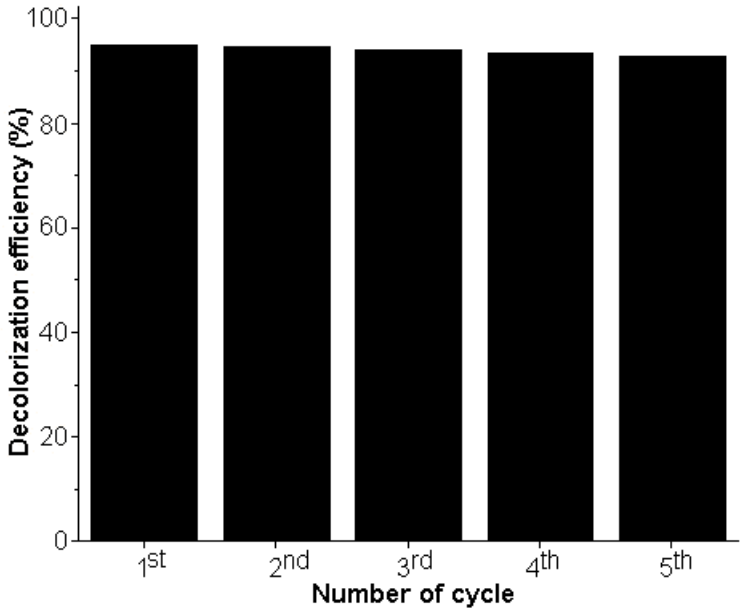

Fig. 11 Photodegradation efficiency of the reused 10% Pt/Bi_2WO_6 nanocomposites in degrading RhB illuminated by visible light for five cycles.

Stability of the photocatalyst is important for the photocatalytic process, therefore the Pt/Bi_2WO_6 photocatalyst was investigated for practical application. The photocatalytic reaction of Pt/Bi_2WO_6 photocatalyst was carried out under visible light for five recycled runs. Fig. 11 shows the photodegradation of RhB over 10% Pt/Bi_2WO_6 nanocomposites. They exhibited a slight loss of photodegradation efficiency at the end of the 5^{th} cycle. Thus, the 10% Pt/Bi_2WO_6 nanocomposites are very stable and are able to withstand corrosion in the extreme condition.

In addition, the stability of reused 10% Pt/Bi_2WO_6 nanocomposites was analyzed by XRD and FTIR as the results shown in Fig. 12. XRD pattern of reused Pt/Bi_2WO_6 nanocomposites was indexed to orthorhombic Bi_2WO_6 structure (JCPDS no. 39-0256 [34]) as a major phase and face centered cubic Pt structure (JCPDS no.

04-0802 [34]) as a minor phase. In this research, the 10% Pt/Bi_2WO_6 nanocomposites were able to withstand photocorrosion under visible light.

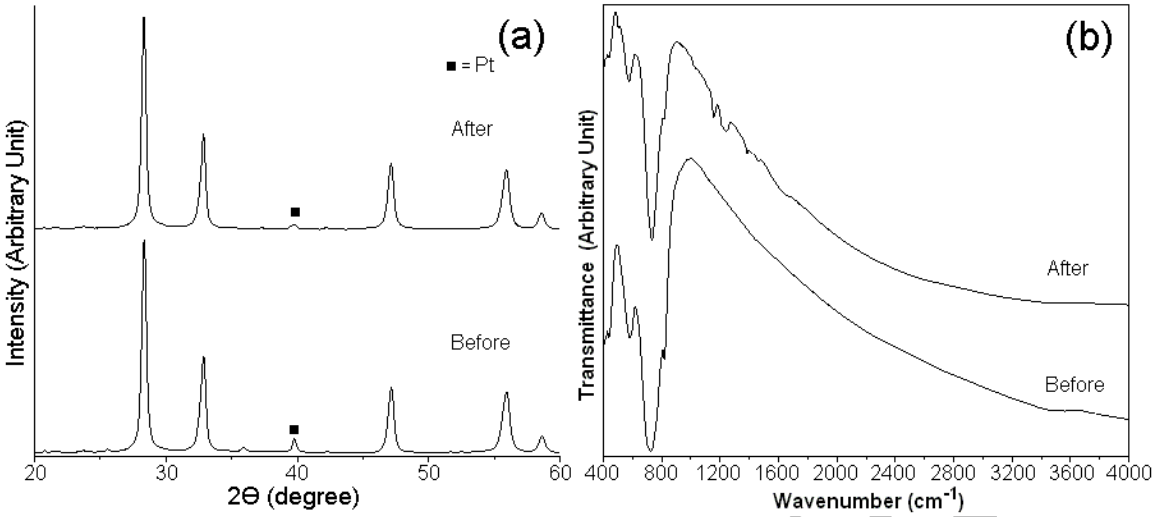

Fig. 12 (a) XRD patterns and (b) FTIR spectra of 10% Pt/Bi_2WO_6 before and after photocatalytic test.

The FTIR spectra of reused 10% Pt/Bi_2WO_6 nanocomposites still show the W–O stretching vibration, Bi–O stretching vibration and asymmetric bridge W–O–W stretching vibration [10, 20, 21, 24, 31, 32]. Additional FTIR peaks at 1000–1500 cm^{-1} belonging to oxygen-functional groups and aromatic structure of RhB molecules were detected because the RhB molecules were adsorbed on top of the Pt/Bi_2WO_6 nanocomposites [56-58]. Therefore, the heterostructure Pt/Bi_2WO_6 nanocomposites are the candidate photocatalyst in degrading RhB dye under visible radiation.

4. Conclusions

In this research, the FCC metallic Pt nanoparticles fully supported on the surface of orthorhombic Bi_2WO_6 thin nanoplates to form the heterostructure Pt/Bi_2WO_6 nanocomposites were successfully prepared by sonochemical-assisted deposition method. The 10% Pt/Bi_2WO_6 nanocomposites have the photocatalytic reaction higher than the Bi_2WO_6 thin nanoplates. According to the trapping experiment, h^+ and $^{\bullet}O_2^-$ are the main active species for RhB degradation in the presence of heterostructure 10% Pt/Bi_2WO_6 nanocomposites illuminated by visible light. The recycled test of heterostructure 10% Pt/Bi_2WO_6 nanocomposites are long-term use for the practical application of photocatalysis.

CRediT authorship contribution statement

S. Pinchujit: Data curation, Formal analysis. A. Phuruangrat: Conceptualization, Methodology, Investigation, Data curation, Formal analysis, Supervision, Writing – review & editing. S. Wannapop: Formal analysis. T. Thongtem: Conceptualization, Formal analysis, Writing – review & editing. S. Thongtem: Conceptualization, Formal analysis, Supervision, Writing – review & editing.

Declaration of competing interest

There are no conflicts of interest to declare.

Acknowledgements

This research was supported by National Science, Research and Innovation Fund (NSRF), Thailand and Prince of Songkla University (grant no. SCI6701032S).

References

1. Yu H., Chu C., An X., Enhanced visible-light-driven photocatalytic activity of F doped reduced graphene oxide-Bi_2WO_6 photocatalyst, *Applied Organometallic Chemistry*, **33(1)**: e4682 (2019).
2. Liu J.Y., Bai Y., Wang P.Q., Photocatalytic degradation of phenol using Au/Bi_2WO_6 composite microspheres under visible-light irradiation, *Nano-Micro Letters*, **8(2)**: 90-93 (2013).
3. Omrani E., Ahmadpour A., Heravi M., Bastami T.R., Novel ZnTi LDH/h-BN nanocomposites for removal of two different organic contaminants: Simultaneous visible light photodegradation of Amaranth and Diazepam, *Journal of Water Process Engineering*, **47**: 102581 (2022).
4. Rafaie H.A., Nazam N.A.A.M., Ramli N.I.T., Mohamed R., Kasim M.F., Synthesis, characterization and photocatalytic activities of Al-doped ZnO for degradation of methyl orange dye under UV light irradiation, *Journal of the Australian Ceramic Society*, **57(2)**: 479-488 (2021).
5. Trinh D.T.T., Channei D., Chansaenpak K., Khanitchaidecha W., Nakaruk A., Photocatalytic degradation of organic dye over bismuth vanadate–silicon dioxide–graphene oxide nanocomposite under visible light irradiation, *Journal of the Australian Ceramic Society*, **56(4)**: 1237-1241 (2020).
6. Zhao G., Hao S., Xing Y., Wang Y., Wang Y., Xu K., Xu X., Preparation of low-dimensional bismuth tungstate (Bi_2WO_6) photocatalyst by electrospinning, *Physica Status Solidi A*, **2016(18)**: 1900035 (2019).
7. Zhu Z., Yan Y., Li J., Synthesis of flower-like WO_3/Bi_2WO_6 heterojunction and enhanced photocatalytic degradation for rhodamine B, *Nano-Micro Letters*, **10(9)**: 460-464 (2015).
8. Lavergne M.A., Chanéac C., Portehault D., Cassaignon S., Durupthy O., Optimized design of Pt-doped Bi_2WO_6 nanoparticle synthesis for enhanced photocatalytic properties, *European Journal of Inorganic Chemistry*, **2016(13-14)**: 2159-2165 (2016).
9. Phuruangrat A., Buapoon S., Bunluesak T., Suebsom P., Thongtem S., Thongtem T., Synthesis of PdAg/Bi_2WO_6 nanocomposites for efficient photodegradation of rhodamine B under visible light irradiation, *Journal of the Australian Ceramic Society*, **58(1)**: 299-307 (2022).
10. Deepthi K., Suresh P., Umabala A.M., Rao A.V.P., Visible light assisted photocatalytic degradation of methyl orange and congo red using Bi_2WO_6 prepared by solid-state metathesis, *Asian Journal of Chemistry*, **30(5)**: 998-1002 (2018).
11. Liu X., Wang S.Z., Wang S., Shi H., Zhang X., Zhong Z., The three-dimensional flower-like Bi_2WO_6 assisted by ethanolamine through a microwave method for efficient photocatalytic activity, *Royal Society Open Science*, **6(3)**: 181422 (2019).
12. Sun S., Wang W., Zhang L., Gao E., Jiang D., Sun Y., Xie Y., Ultrathin {001}-oriented bismuth tungsten oxide nanosheets as highly efficient photocatalysts, *ChemSusChem*, **6(10)**: 1873-1877 (2013).
13. Fu H., Pan C., Yao W., Zhu Y., Visible-light-induced degradation of rhodamine B by nanosized Bi_2WO_6, *Journal of Physical Chemistry B*, **109(47)**: 22432-22439 (2005).

14. He Z., Sun C., Yang S., Ding Y., He H., Wang Z., Photocatalytic degradation of rhodamine B by Bi_2WO_6 with electron accepting agent under microwave irradiation: Mechanism and pathway, *Journal of Hazardous Materials*, **162(2-3)**: 1477-1486 (2009).
15. Selvi M.H., Vanga P.R., Ashok M., Photocatalytic application of Bi_2WO_6 nanoplates structure for effective degradation of methylene blue, *Optik*, **173**: 227-234 (2018).
16. Suryavanshi R.D., Babar P.V., Narewadikar N.A., Rajpure K.Y., Sunlight assisted novel spray deposited Bi_2WO_6 photoelectrode for degradation of organic pollutants, *Journal of Physics and Chemistry of Solids*, **168**: 110786 (2022).
17. Shivani V., Harish S., Archana J., Navaneethan M., Ponnusamy S., Hayakawa Y., Highly efficient 3-D hierarchical Bi_2WO_6 catalyst for environmental remediation, *Applied Surface Science*, **488**: 696-706 (2019).
18. Sun S., Wang W., Xu J., Wang L., Zhang Z., Highly efficient photocatalytic oxidation of phenol over ordered mesoporous Bi_2WO_6, *Applied Catalysis B*, **106(3-4)**: 559-564 (2011).
19. Chen Y., Zhang F., Guan S., Shi W., Wang X., Huang C., Chen Q., Visible light degradation of tetracycline by hierarchical nanoflower structured fluorine-doped Bi_2WO_6, *Materials Science in Semiconductor Processing*, **140**: 106385 (2022).
20. Chu X., Shan G., Chang C., Fu Y., Yue L., Zhu L., Effective degradation of tetracycline by mesoporous Bi_2WO_6 under visible light irradiation, *Frontiers of Environmental Science & Engineering*, **10(2)**: 211-218 (2016).
21. Villa K., Děkanovský L., Plutnar J., Kosina J., Pumera M., Swarming of perovskite-like Bi_2WO_6 microrobots destroy textile fibers under visible light, *Advanced Functional Materials*, **30(51)**: 2007073 (2020).
22. Phuruangrat A., Buapoon S., Bunluesak T., Suebsom P., Wannapop S., Thongtem T., Thongtem S., Hydrothermal preparation of Au-doped Bi_2WO_6 nanoplates for enhanced visible-light-driven photocatalytic degradation of rhodamine B, *Solid State Sciences*, **128**: 106881 (2022).
23. Wang R., Li B., Xiao Y., Tao X., Su X., Dong X., Optimizing Pd and Au-Pd decorated Bi_2WO_6 ultrathin nanosheets for photocatalytic selective oxidation of aromatic alcohols, *Journal of Catalysis*, **364**: 154-165 (2018).
24. Wu Y., Zhang X., Zhang G., Guan W., Visible light-assisted synthesis of Pt/Bi_2WO_6 and photocatalytic activity for ciprofloxacin, *Nano-Micro Letters*, **9(2)**: 119-122 (2014).
25. Bunluesak T., Phuruangrat A., Thongtem S., Thongtem T., Pd nanoparticle-modified Bi_2WO_6 nanoplates used for visible-light-driven photocatalyst, *Research on Chemical Intermediates*, **47(10)**: 4157-4171 (2021).
26. Salari H., Yaghmaei H., Z-scheme 3D Bi_2WO_6/MnO_2 heterojunction for increased photoinduced charge separation and enhanced photocatalytic activity, *Applied Surface Science*, **532**: 147413 (2020).
27. Zhou H., Peng Y., Qin S., Ag@Bi_2WO_6 composites with high visible-light-driven photocatalytic activities prepared in UV light irradiation, *Chinese Journal of Chemistry*, **29(11)**: 2345-2349 (2011).
28. Lin J., Guo Z., Zhu Z., Ag/Bi_2WO_6 plasmonic composites with enhanced visible photocatalytic activity, *Ceramics International*, **40(5)**: 6495-6501 (2014).

29. Phuruangrat A., Maneechote A., Dumrongrojthanath P., Ekthammathat N., Thongtem S., Thongtem T., Visible-light driven photocatalytic degradation of rhodamine B by Ag/Bi_2WO_6 heterostructures, *Materials Letters*, **159**: 289-292 (2015).
30. Bunluesak T., Phuruangrat A., Thongtem S., Thongtem T., Photodeposition of AgPd nanoparticles on Bi_2WO_6 nanoplates for the enhanced photodegradation of rhodamine B, *Inorganic Chemistry Communications*, **124**: 108399 (2021).
31. Phuruangrat A., Keereesaensuk P., Karthik K., Dumrongrojthanath P., Ekthammathat N., Thongtem S., Thongtem T., Synthesis and characterization Ag nanoparticles supported on Bi_2WO_6 nanoplates for enhanced visible-light-driven photocatalytic degradation of rhodamine B, *Journal of Inorganic and Organometallic Polymers and Materials*, **30(4)**: 1033–1040 (2020).
32. Allé P.H., Fanou G.D., Robert D., Adouby K., Drogui P., Photocatalytic degradation of Rhodamine B dye with TiO_2 immobilized on SiC foam using full factorial design, *Applied Water Science*, **10(9)**: 207 (2020).
33. Saigl Z.M., Various adsorbents for removal of rhodamine B dye: A review, *Indonesian Journal of Chemistry*, **21(4)**: 1039-1056 (2001).
34. Powder Diffract. File, JCPDS-ICDD, 12 Campus Blvd., Newtown Square, PA 19073-3273, U.S.A. (2001).
35. Khidirov I., Parpiev A.S., Getmanskii V.V., Makhmudov S.A., Neutron diffraction study of phase transformations at the lower boundary of the homogeneity range of cubic titanium carbide TiC_x, *Russian Journal of Inorganic Chemistry*, **67(4)**: 479-487 (2022).
36. Simonenko T.L., Bocharova V.A., Simonenko N.P., Simonenko E.P., Sevastyanov V.G., Kuznetsov N.T., Formation of $NiMoO_4$ anisotropic nanostructures under hydrothermal conditions, *Russian Journal of Inorganic Chemistry*, **66(12)**: 1779-1784 (2021).
37. Bunluesak T., Phuruangrat A., Thongtem S., Thongtem T., Photocatalytic reaction of heterostructure $Ag_{0.9}Pd_{0.1}/Bi_2WO_6$ nanocomposites to rhodamine B under visible light irradiation, *Digest Journal of Nanomaterials and Biostructures*, **15(3)**: 913-921 (2020).
38. Phuruangrat A., Dumrongrojthanath P., Ekthammathat N., Thongtem S., Thongtem T., Hydrothermal synthesis, characterization, and visible light-driven photocatalytic properties of Bi_2WO_6 nanoplates, *Journal of Nanomaterials*, **2014**: 138561 (2014).
39. Mączka M., Macalik L., Hermanowicz K., Kępínski L., Tomaszewski P., Phonon properties of nanosized bismuth layered ferroelectric material-Bi_2WO_6, *Journal of Raman Spectroscopy*, **41(9)**: 1059-1066 (2010).
40. Maczka M., Hanuza J., Paraguassu W., Filho A.G.S., Freire P.T.C., Filho J.M., Phonons in ferroelectric Bi_2WO_6 : Raman and infrared spectra and lattice dynamics, *Applied Physics Letters*, **92(11)**: 112911 (2008).
41. Karbasi M., Hashemifar S.J., Karimzadeh F., Giannakis S., Pulgarin C., Raeissi K., Sienkiewicz A., Decrypting the photocatalytic bacterial inactivation ofhierarchical flower-like Bi_2WO_6 microspheres induced bysurface properties: Experimental studies and ab initio calculations, *Chemical Engineering Journal*, **427**: 131768 (2022).
42. Ren F., Zhang J., Wang Y., Yao W., Graphene-coupled Bi_2WO_6 nanocomposite with enhanced photocatalytic performance: First-principles study, *Physical Chemistry Chemical Physics*, **18(20)**: 14113-14121 (2016).

43. Jia Z., Lyu F., Zhang L.C., Zeng S., Liang S.X., Li Y.Y., Lu J., Pt nanoparticles decorated heterostructured g-C_3N_4/Bi_2MoO_6 microplates with highly enhanced photocatalytic activities under visible light, *Scientific Reports*, **9(1)**: 7636 (2019).
44. Isyaku U.B., Khir M.H.B.M., Nawi I.M., Zakariya M.A., Zahoor F., ZnO Based resistive random access memory device: A prospective multifunctional next-generation memory, *IEEE Access*, **9**: 105012-105047 (2021).
45. Ziashahabi A., Prato M., Dang Z., Poursalehi R., Naseri N., The effect of silver oxidation on the photocatalytic activity of Ag/ZnO hybrid plasmonic/metal-oxide nanostructures under visible light and in the dark, *Scientific Reports*, **9(1)**: 11839 (2019).
46. Liu W., Jin R., Hu L., Zhong H., Ren L., Hu S., Facile fabrication of Ag–Bi_2GeO_5 microflowers and the high photodegradable performance on RhB, *Journal of Materials Science*, **30(11)**: 10912-10922 (2019).
47. Zheng Z., Liu J., Yu H., Wang Y., Chen C., Wang J., Wang S., Adsorption performance and mechanism of U(VI) in aqueous solution by hollow microspheres Bi_2WO_6, *Journal of Radioanalytical and Nuclear Chemistry*, **332(6)**: 1755–1765, (2023).
48. Liu M., Xue X., Yu S., Wang X., Hu X., Tian H., Chen H., Zheng W., Improving photocatalytic performance from Bi_2WO_6@MoS_2/graphene hybrids via gradual charge transferred pathway, *Scientific Reports*, **7(1)**: 3637 (2017).
49. Wang M., Qiao Z., Fang M., Huang Z., Liu Y., Wu X., Tang C., Tang H., Zhu H., Synthesis of Er-doped Bi_2WO_6 and enhancement in photocatalytic activity induced by visible light, RSC Advances, **5(115)**: 94887-94894 (2015).
50. Pinchujit S., Phuruangrat A., Wannapop S., Sakhon T., Kuntalue B., Thongtem T., Thongtem S., Synthesis and characterization of heterostructure Pt/Bi_2WO_6 nanocomposites with enhanced photodegradation efficiency induced by visible radiation, Solid State Sciences, **134**: 107064 (2022).
51. Chen L., Feng X., Synthesis and characterization of V_2O_5/$BiVO_4$ cake-like microstructures, Journal of the Australian Ceramic Society, **55(4)**: 1067-1074 (2019).
52. Dong B., Yu X., Dong Z., Yang X., Wu Y., Facile synthesis of ZnO nanoparticles for the photocatalytic degradation of methylene blue, *Journal of Sol-Gel Science and Technology*, **82(1)**: 167-176 (2017).
53. Wang Y., Zeng Y., Zhang S., Zhong Q., Synthesis of 3D hierarchical rose-like Bi_2WO_6 superstructure with enhanced visible-light-induced photocatalytic performance, *JOM*, **71(6)**: 2112-2119 (2019).
54. Niu Z. Guo S., Li J., Q. F., W. J., Yang C., Gao C., Zhou J., Liu Z., Sun H., Wang X., Hydrothermal synthesis of $LaCoO_3$ perovskite catalyst and its application for the degradation of phenol under visible light, *Iranian Journal of Chemistry and Chemical Engineering*, **42(6)**: 1744-1757 (2023).
55. Cheng T., Chen C., Ye C., Xie W., Zhang X. Tian, Y., Synthesis of $KBiO_3$/nano-Ag_3PO_4 composite photocatalyst and its application for degradation of organic pollutants under visible light, *Iranian Journal of Chemistry and Chemical Engineering*, **41(6)**: 1942-1960 (2022).
56. Ano T., Kishimoto F., Tsubaki S., Lu Y.H., Hohman J.N., Maitani M.M., Salmeron M., Wada Y., Controlling the Schottky barrier at the Pt/TiO_2 interface by intercalation of a self-assembled monolayer with oriented dipole moments, *Journal of Physical Chemistry C*, **125(25)**: 13984-13989 (2021).

57. Sydorchuk V., Poddubnaya O.I., Tsyba M.M., Zakutevskyy O., Khyzhun O., Khalameida S., Puziy A.M., Activated carbons with adsorbed cations as photocatalysts for pollutants degradation in aqueous medium, *Adsorption*, **25(3)**: 267–278 (2019).
58. Liu H., Xu C., Wei X., Ren Y., Tang D., Zhang C., Zhang R., Li F., Huo C., 3D hierarchical porous activated carbon derived from bamboo and its application for textile dye removal: Kinetics, isotherms, and thermodynamic studies, *Water, Air, and Soil Pollution*, **231(10)**: 504 (2020).